Corrosion Science 103 (2016) 124–131

Contents lists available at ScienceDirect

Corrosion Science

journal homepage: www.elsevier.com/locate/corsci

Oxidation of ferritic and ferritic–martensitic steels in flowing and static supercritical water

Nai-qiang Zhang[a,b], Zhong-liang Zhu[a], Hong Xu[a,*], Xue-ping Mao[a], Ju Li[b,*]

[a] Key Laboratory of Condition Monitoring and Control for Power Plant Equipment of Ministry of Education, North China Electric Power University, Beijing 102206, PR China

[b] Department of Nuclear Science and Engineering and Department of Materials Science and Engineering, Massachusetts Institute of Technology, Cambridge, MA 02139, United States

ARTICLE INFO

Article history:
Received 23 May 2015
Received in revised form 28 August 2015
Accepted 14 October 2015
Available online 19 October 2015

Keywords:
A. Steel
B. SEM
B. XRD
C. Oxidation

ABSTRACT

The oxidation of ferritic steel and ferritic–martensitic steel was investigated by exposure to flowing and static supercritical water (SCW) at 550–600 °C. The oxidation kinetic curves follow parabolic and near-cubic rate equations for the samples exposed to flowing and static SCW, respectively. The phase analysis shows the presence of hematite, magnetite and spinel in flowing SCW while only the magnetite and spinel phases are identified in static SCW. The mechanism of the formation of hematite and the effect of the flow state of SCW on the time exponent of oxidation kinetics are discussed.

1. Introduction

The supercritical water reactor (SCWR) is one of the most promising advanced reactor concepts for Generation IV nuclear reactors because of its high efficiency and simple design [1,2]. However, when operating above the thermodynamic critical point of water (374 °C/22.1 MPa), supercritical water (SCW) is expected to be more corrosive to conventional structural materials. Thus, the oxidation behaviour of materials at SCW conditions has been one of the main issues under investigation [3,4].

Ferritic/martensitic steels have been widely studied and developed for applications in the energy industry, generally because of their high thermal conductivity and lower thermal expansion coefficients [5]. Wright and Pint [6] summarized the high-temperature oxidation behaviour of HCM12A and NF616 in water vapour and steam, which showed that the oxidation kinetics follow the parabolic rate equation at temperatures up to 700 °C. Yin et al. [7] studied the oxidation of P92 in static supercritical water at 500–600 °C and claimed that the oxidation rates at three different temperatures follow the near-cubic rate equation. Zhang et al. [8] investigated the oxidation behaviour of P92 in static SCW containing different dissolved oxygen (DO) and found that the weight gains increase with the DO concentration from 100 to 2000 part-per-billion (ppb) in weight at 550 °C and follow a near-cubic rate equation. The experiments on the oxidation behaviour of T91, T92, HT9 and HCM12A were performed in SCW at 500 °C with DO from 25 to 2000 ppb [9–15]. The above experiments were conducted either in flowing or in static SCW. Without distinguishing the influence of the flow state on the oxidation behaviour, it is difficult to compare and understand the oxidation kinetics and the oxide composition.

The oxidation behaviour of ferritic steel T22 and ferritic–martensitic steel P92 in flowing and static SCW at 550–600 °C under 25 MPa with a DO content of 2 part-per-million (ppm) in weight was investigated in this paper. The chemical compositions of T22 and P92 are given in Table 1. The mechanism of the influence of flowing and static SCW on the oxidation kinetics and oxide composition is also discussed.

2. Experimental

The bulk T22 and P92 steels were cut into samples with a size of 25 mm × 10 mm × 2 mm. The samples were polished using 1 μm diamond paste and were cleaned in acetone and deionized water.

Oxidation tests in flowing SCW at 550–600 °C were performed in a continuous SCW experimental facility at a pressure of 25 MPa with a DO content of 2 ppm and a water flow rate of 5 ml/min through a 5 cm^2 area cross-section. Fig. 1 shows the schematics of the SCW

* Corresponding authors. Fax: +86 10 61773877.
E-mail addresses: xuhong@ncepu.edu.cn (H. Xu), liju@mit.edu (J. Li).

http://dx.doi.org/10.1016/j.corsci.2015.10.017
0010-938X/

Table 1
Chemical composition of the alloys (wt.%).

Alloy	C	Si	Mn	S	P	Cr	Mo	W	V	Nb	Ni	Cu	N	Al	B	Fe
T22	0.12	0.5	0.6	0.025	0.025	2.25	0.54	–	–	–	–	–	–	–	–	Bal.
P92	0.10	0.38	0.42	0.001	0.014	8.63	0.37	1.59	0.164	0.053	0.15	0.09	0.0385	0.02	0.0013	Bal.

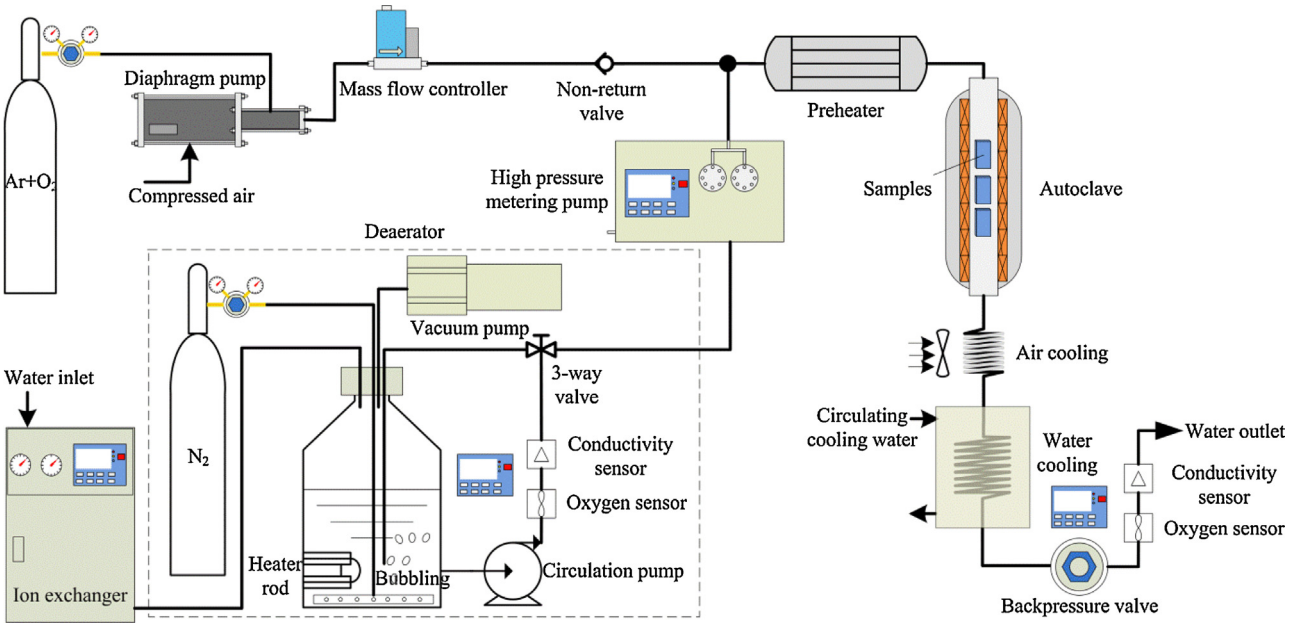

Fig. 1. Schematic diagram of the supercritical water oxidation testing facility.

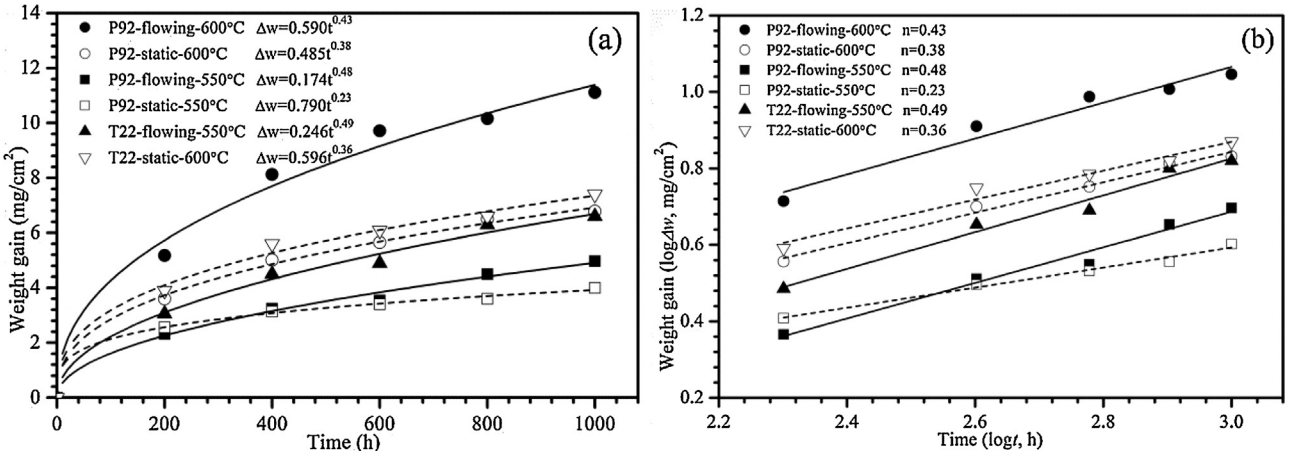

Fig. 2. Weight gain changes as a function of exposure time for T22 and P92 samples after exposure to flowing or static supercritical water containing 2 ppm dissolved oxygen at 550–600 °C under 25 MPa. The solid symbols and lines represent the experimental data exposed to flowing supercritical water. The open symbols and dashed lines represent the experimental data exposed to static supercritical water. The experimental data of P92 in 550 °C static supercritical water are from Ref. [8].

experimental facility. Ultrapure water with an electrical conductivity of less than 0.1 μS/cm was obtained using an ion exchanger. The working medium water was deaerated by heating to 100 °C and bubbling with pure nitrogen gas. The DO content in the reaction system was controlled by injecting mixed argon and oxygen gas, and it was corrected by a mass flow controller according to the DO sensor behind the backpressure valve. The flow rate and pressure were controlled through the high pressure metering pump and the backpressure valve. Samples were placed in the autoclave using platinum wires and ceramic insulators to avoid galvanic effects. The oxidation tests in static SCW at 550–600 °C were performed in a static autoclave. The controlling methods for the DO content, pressure and temperature were described elsewhere [8,16].

All exposure experiments were performed at 550 ± 3 °C or 600 ± 3 °C under a pressure of 25 ± 0.2 MPa. The exposure periods were 200, 400, 600, 800 and 1000 h. In each test, the samples with a short exposure time were removed after their designed exposure period. The samples with a longer exposure period were cooled to room temperature (as part of the samples exchange) and reheated to the designed testing temperature to finish the rest of the exposure. The samples were weighed before and after exposure using a METTLER TOLEDO milligram balance with a sensitivity of 0.1 mg. The morphology and chemical compositions of the oxide films were analyzed with a JEOL JSM 6490LV scanning electron microscope (SEM) equipped with an OXFORD Instrument INCA energy dispersive X-ray spectrometer (EDS). A theta—2θ PANALYTICAL

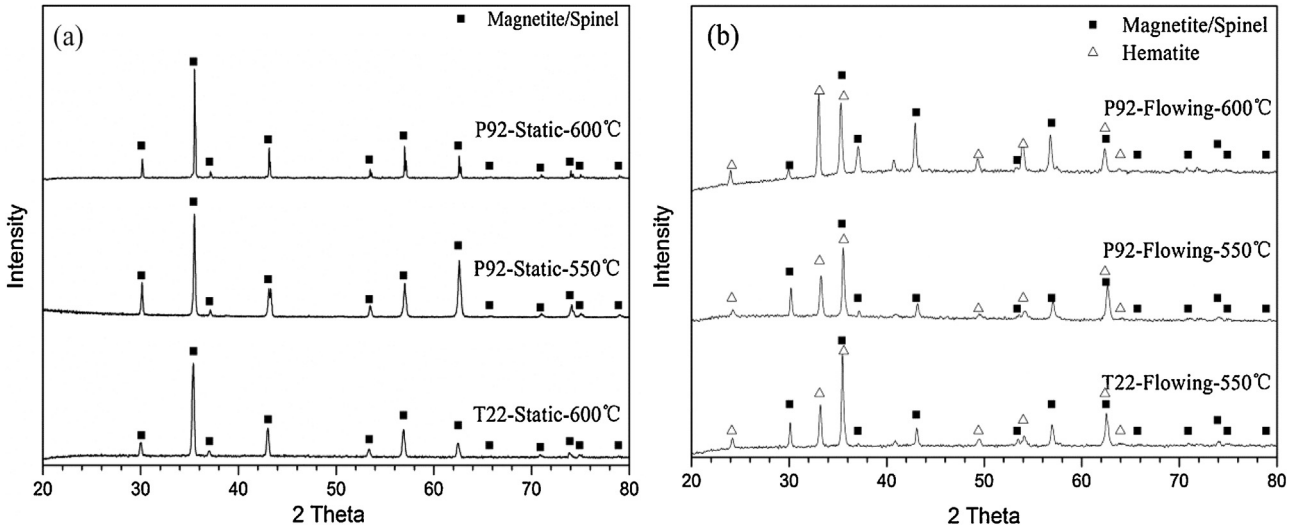

Fig. 3. The XRD patterns of T22 and P92 samples exposed to (a) static and (b) flowing supercritical water containing 2 ppm dissolved oxygen under 25 MPa for 1000 h.

X-ray diffraction (XRD) was employed to determine the crystal structure of the oxides.

3. Results and analysis

3.1. Weight gain

The relation of the weight gain and the exposure time can be expressed as:

$$\Delta w = k_0 \exp\left(-\frac{E}{RT}\right) t^n = k_p t^n \quad (1)$$

where Δw is the weight gain of alloys per unit area, E is the activation energy for oxidation, k_p and k_0 are the oxidation rate constants, R is the ideal gas constant, T is the exposure temperature in Kelvin, t is the exposure time in hours and n is the time exponent that describes the time dependence of oxide growth. The weight gains as a function of time for T22 and P92 exposed to SCW at 550–600 °C under 25 MPa are shown in Fig. 2.

The curves show that the weight gain increases with exposure time. Both T22 and P92 exposed to flowing SCW at 550–600 °C obey a parabolic rate equation ($n = 0.5$). In contrast, the weight gain of P92 exposed to 550 °C static SCW (dotted line) [8] is closer to a cubic rate equation. Moreover, the weight gains of T22 and P92 in 600 °C static SCW are similar to the cubic rate equation. The oxidation rate of P92 is slower than T22, which can be explained by the higher concentration of Cr in P92 leading to the formation of a more protective oxide layer.

3.2. Surface morphology and structure

As shown in Fig. 3, the oxide phases of the T22 and P92 after exposure to 2 ppm DO SCW at 550–600 °C for 1000 h were identified using XRD. The diffraction results in flowing SCW show the presence of hematite, magnetite and spinel. However, only the magnetite and spinel are identified in static SCW. The XRD and SEM/EDS analyses show that the phase composition of the oxide layers is different in flowing and static SCW. The three-phase structure with hematite, magnetite and spinel is detected by EDS in flowing SCW, in accordance with others reports [9,10].

The surface morphology of the T22 and P92 samples exposed to 550–600 °C SCW water with 2 ppm DO content for 200, 600 and 1000 h are shown in Fig. 4. Porosities can be observed on the top of the oxide layer (Fig. 4) and on the cross-section of the oxide layer (Figs. 5 and 6). On the top of the oxide layer, the porosity decreases as a function of time (Fig. 4), which is in agreement with the literature results [9]. In the cross-sectional observations, porosities are also observed, in agreement with the literature [11]. According to Ref. [17], they are formed by vacancies accumulation in the magnetite layer. Maruyama et al. [18] and Ueda et al. [19] proposed that void formation and healing in a growing oxide scale formed in the high temperature oxidation of metals could be explained by the iron and oxygen diffusivities that depend on the oxygen chemical potential, the fluxes of ions and the sign of their divergences. These pores can act as short circuit paths for the transportation of oxygen [20]. A marker experiment revealed that the outer and inner oxide layers grow predominantly by the outward migration of iron and the inward migration of oxygen, respectively [21], which are affected by the short circuit paths, such as pores, cracks and grain boundaries [12,22,23]. Fig. 4 shows that micro cracks and large cracks in the oxide scales formed on the samples exposed to 600 °C for 600 h and 1000 h but 550 °C. Growth stress may accumulate and cause crack initiation and propagation through the growing oxide scale, which would increase the effective diffusivity with time.

3.3. Oxide layer structure (SEM/EDS)

The cross-sectional morphology and the corresponding composition profiles of the T22 and P92 samples exposed to SCW at 550 °C and 600 °C for 200, 600 and 1000 h are shown in Figs. 5 and 6. The oxide scale is mainly composed of two different layers and a transition region between the inner oxide layer and the substrate. According to the morphology and EDS analysis, the inner layer is a compact Cr-rich spinel, in which the Cr concentration is approximately equal to that of the substrate alloy, whereas the outer layer is a porous Fe-rich oxide [7,8,10,24]. A thin transition layer is observed, in which Fe concentration gradually changes from that of the oxide to the bulk alloy concentration, Cr concentration maintains the bulk alloy concentration while O concentration gradually changes from that of the oxide to zero. Compared with the previous paper [8], the thickness of the oxide scales for P92 exposed to flowing SCW is greater, which indicates that the oxidation rate in flowing SCW is higher than in static SCW. As reported in Refs. [15,25], the interface between the outer layer and the inner layer coincides with the original metal surface. Based on the mass balance and the assumption that no iron was released into the SCW, all of the iron that diffused from the substrate is fixed in the outer and the inner layer. All of the chromium oxidized from the substrate is

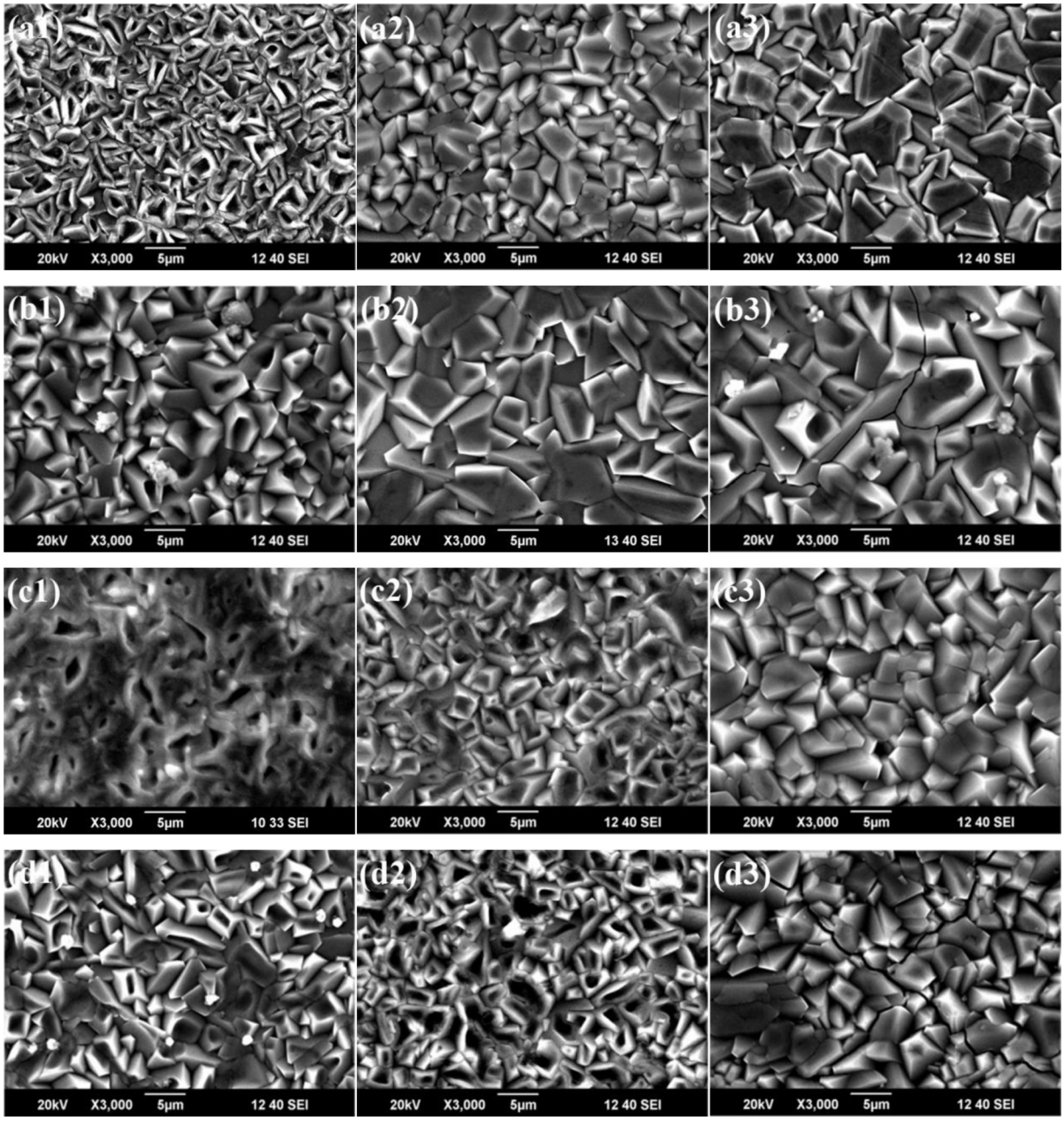

Fig. 4. SEM images showing the surface morphologies of the oxide scales formed on T22 and P92 after exposure to flowing SCW at 550 °C and static SCW at 600 °C containing 2 ppm dissolved oxygen under 25 MPa for 200, 600 and 1000 h, respectively: (a1) T22, 550 °C for 200 h, (a2) T22, 550 °C for 600 h, (a3) T22, 550 °C for 1000 h, (b1) T22, 600 °C for 200 h, (b2) T22, 600 °C for 600 h, (b3) T22, 600 °C for 1000 h, (c1) P92, 550 °C for 200 h, (c2) P92, 550 °C for 600 h, (c3) P92, 550 °C for 1000 h, (d1) P92, 600 °C for 200 h, (d2) P92, 600 °C for 600 h, (d3) P92, 600 °C for 1000 h.

found in the inner layer. The thickness ratio of the outer layer and the inner layer can be expressed by

$$\frac{h_{out}}{h_{in}} = \frac{x\left(1 + C_{Fe}/C_{Cr}\right)}{3} - 1 \quad (2)$$

where h_{out} and h_{in} are the thickness of the outer and the inner oxide layers (μm), respectively. C_{Fe} and C_{Cr} are the chromium and iron concentrations in the alloy (mol/cm^3). The Fe–Cr spinel can be expressed as $Fe_{3-x}Cr_xO_4$, where x denotes the stoichiometric number. According to the values in Table 1, the C_{Fe}/C_{Cr} ratios of T22 and P92 are 39.6 and 9.5, respectively. Based on the EDS results, the average Fe/Cr atomic ratios of the inner layer are approximately 16:1 and 4:1 for T22 and P92, respectively. The x values for T22 and P92 obtained from the EDS results are 0.2 and 0.6, respectively. These stoichiometries remain constant during the whole oxidation process and through the Fe–Cr spinel layer [26]. The theoretical thickness ratios of the outer to the inner oxide layer for T22 and P92 are 1.39 and 1.1, as estimated by Eq. (2). The experimental values are presented in Fig. 7 at different exposure times and temperatures. The experimental thickness ratio tends to increase with exposure time and is slightly less than the corresponding theoretical value. This may be contributed to inward oxygen diffusion to form a thin Fe/Cr layer at the initial oxidation stage, which doesn't involve outward diffusion of cations across the oxide layer. However, the influence of the initial oxidation stage becomes increasingly smaller with the increasing time.

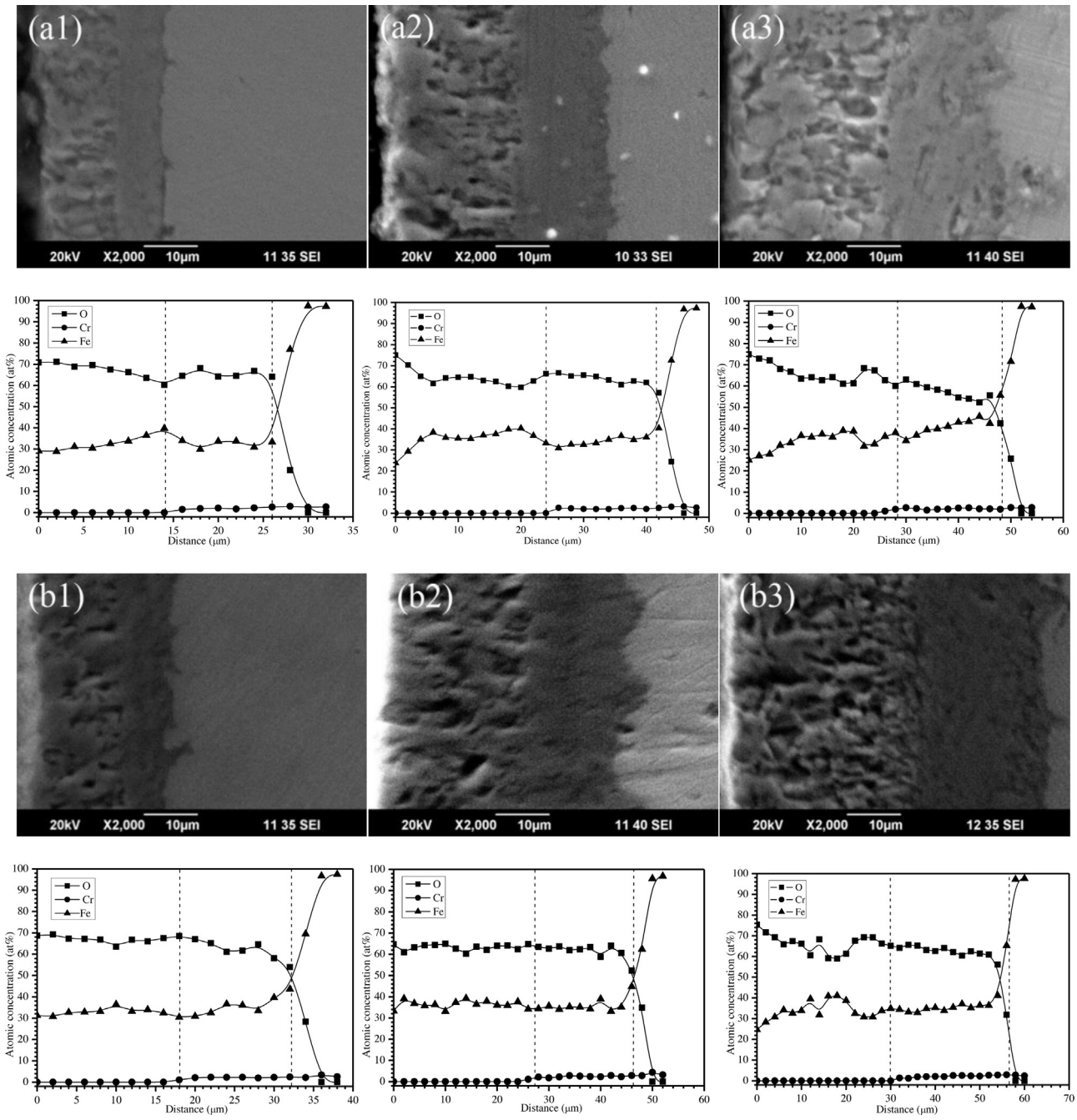

Fig. 5. The cross-sectional SEM images of the oxides and the corresponding elemental depth profiles of T22 exposed to flowing SCW at 550 °C and static SCW at 600 °C containing 2 ppm dissolved oxygen under 25 MPa for 200, 600 and 1000 h, respectively. The dashed vertical lines are used to demarcate the interfaces between the Fe-rich outer layer, the Cr-rich inner layer and the transition layer. (a1) 550 °C for 200 h, (a2) 550 °C for 600 h, (a3) 550 °C for 1000 h, (b1) 600 °C for 200 h, (b2) 600 °C for 600 h, (b3) 600 °C for 1000 h.

Distinct gaps are observed at the interfaces between the inner oxide layer and the substrate for 1000 h at 550 °C and for 600 and 1000 h at 600 °C. In contrast, no gap is found on the T22 samples in all cases. The formation of gaps and oxide exfoliation are related to the internal stress between the oxide and the substrate. This internal stress originates from the growth stress when the oxides form on specimens due to the Pilling–Bedworth ratio, as well as the thermal stress during temperature changes due to the difference of the thermal expansion coefficients between the oxides and the substrate. The main reason for the difference of gaps between the P92 and T22 samples is the different chromium concentrations of the spinel oxides formed on their surface.

4. Discussion

4.1. Effect of the chromium concentration

Many oxidation mechanisms of ferritic/martensitic steels in SCW have been proposed in recent years [5,7,9,15]. It is assumed that the outer layer grows at the oxide/water interface due to the transport of Fe ions through the inner oxide layer, and the Cr-rich spinel oxide grows at the oxide/metal interface due to the inward transport of oxygen and water [27,28]. Furthermore, the oxidation rate-controlling step for the oxidation of ferritic/martensitic steels is the outward diffusion of Fe ions through the inner layers

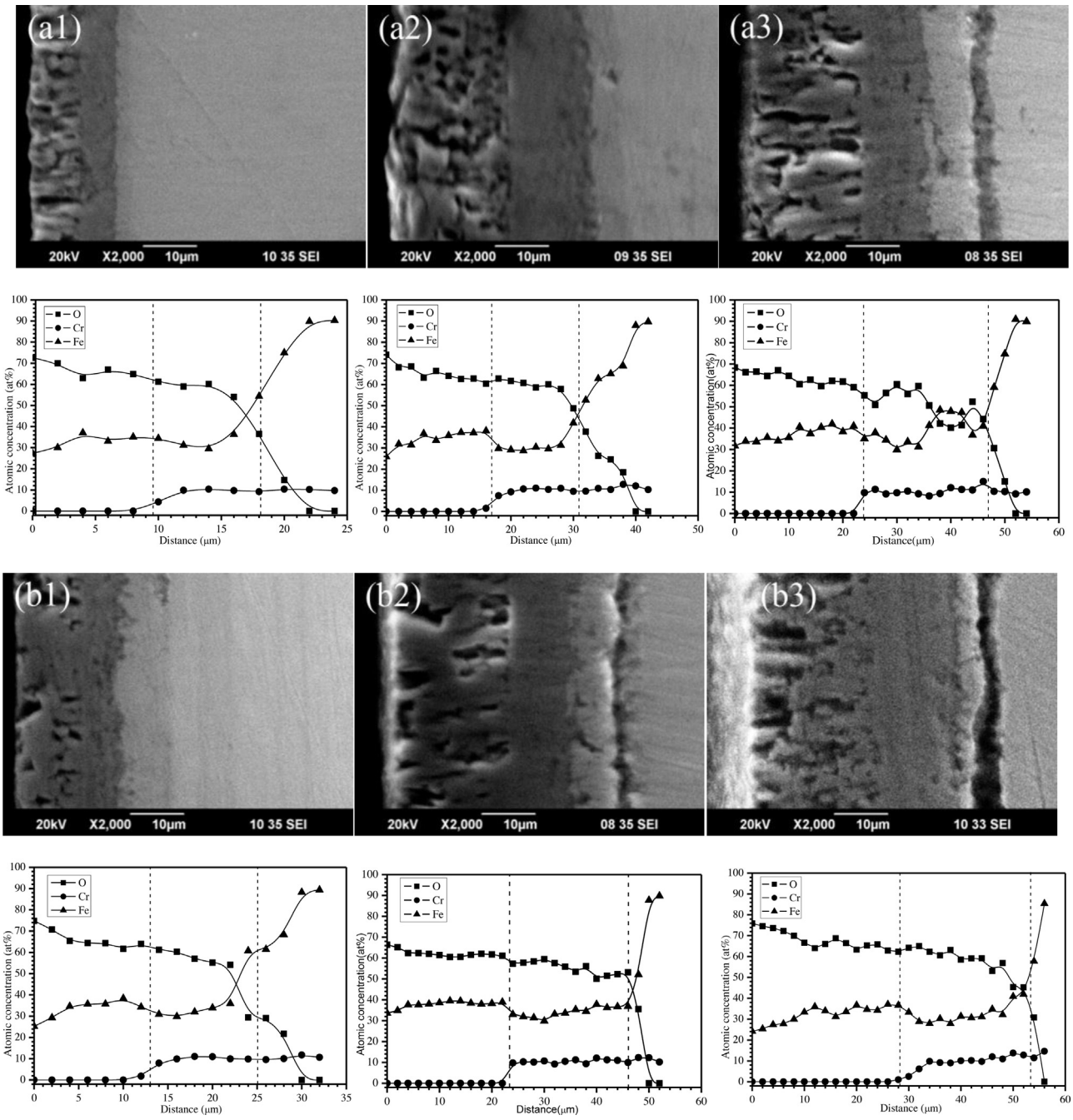

Fig. 6. The cross-sectional SEM images of the oxides and the corresponding elemental depth profiles of P92 exposed to flowing SCW at 550 °C and static SCW at 600 °C containing 2 ppm dissolved oxygen under 25 MPa for 200, 600 and 1000 h, respectively. The dashed vertical lines are used to demarcate the interfaces between the Fe-rich outer layer, the Cr-rich inner layer and the transition layer. (a1) 550 °C for 200 h, (a2) 550 °C for 600 h, (a3) 550 °C for 1000 h, (b1) 600 °C for 200 h, (b2) 600 °C for 600 h, (b3) 600 °C for 1000 h.

[26,28,29], which is consistent with the presence of the transition layer in the samples. If the diffusion of oxygen were the oxidation rate-controlling step, the significant transition layer would not form because oxygen would not be able to diffuse far ahead of the oxide [15]. In Robertson's [30,31] model for aqueous oxidation, it is assumed that the corrosion rate is limited by cation diffusion in the inner layer. This assumption is reasonable because the Fe-tracer diffusion coefficient decreases with the increasing Cr concentration in the Fe–Cr spinel [32]. This assumption was also proven by Martinelli's experiment [29]. Generally speaking, the higher the Cr concentration is, the lower the oxidation rate is [33]. The Cr-rich spinel plays a decisive role in the oxidation rate of the metal. In this paper, the weight gain curves show that the weight gain of T22 is higher than that of P92 at 550 °C and 600 °C, which is due to the lower chromium concentration of the spinel layer of T22.

4.2. Influence of the oxidation environments (flowing vs. static)

Parabolic oxidation kinetics is usually employed when the effective diffusivities of the reactants are independent of time and length scales. As discussed above, the oxidation mechanism of the ferritic/martensitic steels in SCW is governed by the outward diffusion of Fe ions and the variations of the oxygen potential. As a result, the oxidation rate might follow the parabolic rate equation with the rate constant predicted by Wagner theory [34] if the oxide layer were flawless and bulk diffusion were dominant. However,

Table 2
A summary of exposure tests in 500–600 °C flowing or static SCW containing different dissolved oxygen contents.

Temperature	Alloys	DO (ppb)	Oxide composition	Time exponent	SCW condition
500 °C	HCM12A	10	$Fe_3O_4/(Fe,Cr)_3O_4$	0.43 [21]	Flowing
	NF616			0.48 [21]	Flowing
	HCM12A	25	$Fe_3O_4/(Fe,Cr)_3O_4$	0.497 [36]	Flowing
	NF616			0.486 [36]	Flowing
	P92	10	$Fe_3O_4/(Fe,Cr)_3O_4$	0.28 [7]	Static
	T91	25	$Fe_3O_4/(Fe,Cr)_3O_4$	0.40 [9]	Flowing
		2000	$Fe_2O_3/Fe_3O_4/(Fe,Cr)_3O_4$	0.57 [9]	Flowing
	HCM12A	2000	$Fe_2O_3/Fe_3O_4/(Fe,Cr)_3O_4$	0.35 [11]	Flowing
	HT9	2000	$Fe_2O_3/Fe_3O_4/(Fe,Cr)_3O_4$	0.44 [10]	Flowing
550 °C	P92	10	$Fe_3O_4/(Fe,Cr)_3O_4$	0.32 [7]	Static
		100		0.28 [8]	Static
		300		0.32 [8]	Static
		2000		0.23 [8]	Static
		2000	$Fe_2O_3/Fe_3O_4/(Fe,Cr)_3O_4$	0.48 (this paper)	Flowing
	T22	2000	$Fe_2O_3/Fe_3O_4/(Fe,Cr)_3O_4$	0.49 (this paper)	Flowing
600 °C	HCM12A	25	$Fe_3O_4/(Fe,Cr)_3O_4$	0.418 [36]	Flowing
	NF616			0.451 [36]	Flowing
	HCM12A			0.457 [24]	Flowing
	P92	10	$Fe_3O_4/(Fe,Cr)_3O_4$	0.31 [7]	Static
		2000		0.38 (this paper)	Static
		2000	$Fe_2O_3/Fe_3O_4/(Fe,Cr)_3O_4$	0.43 (this paper)	Flowing
	T22	2000	$Fe_3O_4/(Fe,Cr)_3O_4$	0.36 (this paper)	Static

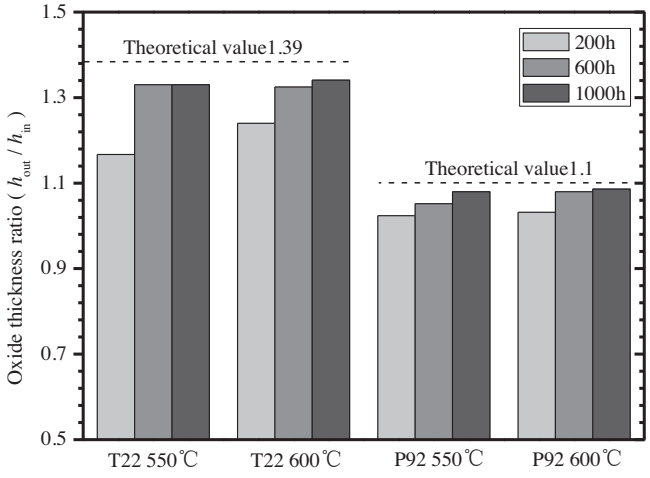

Fig. 7. Comparison of the oxide thickness ratio of the outer to inner layer for T22 and P92 exposed to flowing SCW at 550 °C and static SCW at 600 °C containing 2 ppm dissolved oxygen for 200, 600 and 1000 h, respectively. The dashed horizontal lines indicate theoretical value.

deviation from the expected parabolic oxidation kinetics is often observed in the SCW environment [7,8]. A summary of these corrosion experiments in SCW is given in Table 2. The oxidation kinetic curves are classified into two groups, that is, a parabolic rate equation ($n = 0.5$) and a cubic rate equation ($n = 0.33$). The oxidation kinetics is more apt to follow the near-cubic rate equation in static SCW and the near-parabolic rate equation in flowing SCW. Whether SCW is static or flowing can influence the oxidation kinetics of metals. Young [35] concluded that surface reactions in bi- and multi-oxidant systems can cause a boundary layer, in which the exposure conditions at the surfaces are different from those in the bulk fluid. In the process of oxidation, hydrogen is formed from water decomposition and metal oxidation in SCW. The generated hydrogen is swept away when SCW is flowing, which makes the DO content (oxygen partial pressure) at the SCW/oxide surface much closer to that in the bulk fluid.

The flow state of SCW (flowing or static) has an impact on the accumulation of hydrogen, thereby affecting the oxygen partial pressure at the SCW/oxide surface. The effective diffusivity of Fe ions and the concentration of defects in oxides are functions of the oxygen partial pressure. For the static SCW condition, the accumulation of hydrogen can lead to a decrease in the oxygen partial pressure at the SCW/oxide surface with increasing oxidation time. Thus, less oxygen can diffuse through the oxide, decreasing the oxygen potential throughout the layers. As a result, the diffusion rate of Fe ions decreases with decreasing oxygen partial pressure, leading to a decrease in the oxidation rate, which is associated with oxidation time. On the other hand, the presence of voids creates short-circuit diffusion paths, which can influence the overall transport through the oxide layer. However, these voids are gradually healed over time (Section 3.2), removing some of the short-circuit diffusion paths, resulting in a decrease of the effective diffusivity with time (the parabolic law assumes constant diffusivity, neglecting the effect of the evolving internal microstructure on the scale's effective diffusivity with time). As a result, the time dependence of the oxidation kinetics deviates from the parabolic rate equation.

4.3. Oxide phase analysis

As shown in Table 2, hematite appears only when SCW is flowing and when the dissolved oxygen content is high enough (2 ppm). At present, there are two possible explanations for the formation of hematite. One is that a high DO content can cause high oxygen partial pressure at the SCW/oxide surface. When the oxygen partial pressure is high enough, the following reaction of the dissolved oxygen in SCW and the Fe ions in the matrix occurs at the surface of the samples in the initial oxidation stage.

$$4Fe + 3O_2 = 2Fe_2O_3 \quad (3)$$

The other explanation is that with the growth of the oxide layer, the outward diffusion of Fe ions through the layer becomes slower, which causes the content of Fe ions on the SCW/oxide surface to decrease. Consequently, magnetite is converted to hematite by the following reaction [37–39].

$$4Fe_3O_4 + O_2 = 6Fe_2O_3 \quad (4)$$

Most of the laboratory tests were shorter than 1000 h, so Fe_2O_3 was not found in low-DO SCW. However, Zhong et al. [40] reported an investigation on a T91 superheater tube after 12,956 h of service in a USC power plant operating in low-DO SCW. They found that the outer layer of the oxide scale is Fe_3O_4 plus some Fe_2O_3. Lee et al. [41] concluded that the outer layer was 95% magnetite and 5% hematite on a T91 superheater tube after operating time of 14,186 h. Moreover, the hematite mass fraction increased with the

increasing oxidation time under low DO. Based on the long-term service results in power plants and laboratory investigations, it can be inferred that when the thickness of the oxide becomes thick enough and the void content formed in the oxide scale is increased to a certain extent, the content of Fe ions that can diffuse outward to the SCW/oxide surface decreases and causes the formation of Fe_2O_3 under low DO. The thermodynamic calculations of the equilibrium (dissociation) oxygen partial pressure of hematite at 550 °C and 600 °C are 1.07×10^{-17} and 6.96×10^{-16} atm, respectively. Although the oxygen partial pressure in the SCW with different DO contents is sufficient to form hematite, the oxygen partial pressure is sensitive to the presence of even a small amount of hydrogen and the consumption rates of oxygen at the SCW/oxide surface. Thus, the SCW state (flowing or static) plays an important role in the oxide composition. The oxygen partial pressure at the SCW/oxide surface is a function of the flow state of SCW, the DO content and the oxidation rate constant. The oxygen partial pressure increases with increasing flow rate of SCW and/or DO content and decreases with increasing oxidation rate constant.

5. Conclusion

The influence of SCW environment (flowing or static) on corrosion behaviour of ferritic and ferritic–martensitic steels exposed to 550–600 °C SCW containing 2 ppm dissolved oxygen was investigated. The thickness ratio of the outer to inner oxide layer depends on the chromium concentration in the alloys. The flow state of SCW can influence the time exponent of the oxidation kinetics and oxide compositions. The oxidation kinetics is prone to follow the near-parabolic rate equation in flowing SCW but the near-cubic rate equation in static SCW. The main difference between flowing and static SCW is the hydrogen and oxygen partial pressures on the SCW/oxide surface, which affect the internal microstructure evolution and result in deviation from the parabolic rate equation.

Acknowledgments

This paper was supported by National Natural Science Foundation of China (51134016, 51471069, 51201064), Beijing Municipal Natural Science Foundation (2152029) and the Fundamental Research Funds for the Central Universities. NQZ acknowledges support by China Scholarship Council 201206735010. J.L. acknowledges support by NSF DMR-1120901.

References

[1] A Technology Roadmap for Generation IV Nuclear Energy Systems, in: US DOE Nuclear Energy Research Advisory Committee and the Generation IV International Forum (GIF-002-00), 2002.
[2] Generation IV roadmap R&D scope report for water cooled reactor systems, in: US DOE Nuclear Energy Research Advisory Committee and the Generation IV International Forum (GIF-003-00), 2002.
[3] S. Teysseyre, J. McKinley, G.S. Was, D.B. Mitton, H. Kim, J.-K. Kim, R.M. Latanision, Proceedings of the 11th International Symposium on Environmental Degradation of Materials in Nuclear Power Systems-Water Reactors, Stevenson, Washington August 10–14, 2004, pp. 63–72.
[4] D. Squarer, T. Schulenberg, D. Struwe, Y. Oka, D. Bittermann, N. Aksan, C. Maraczy, R. Kyrki-Rajamäki, A. Souyri, P. Dumaz, High performance light water reactor, Nucl. Eng. Des. 221 (2003) 167–180.
[5] R. Viswanathan, J. Sarver, J.M. Tanzosh, Boiler materials for ultra-supercritical coal power plants—steamside oxidation, J. Mater. Eng. Perform. 15 (2006) 255–274.
[6] I.G. Wright, B.A. Pint, An assessment of the high-temperature oxidation behavior of Fe–Cr steels in water vapor and steam, in: NACE Oxidation, Denver, CO, April 8–11, 2002, paper No. 2377.
[7] K. Yin, S. Qiu, R. Tang, Q. Zhang, L. Zhang, Corrosion behavior of ferritic/martensitic steel P92 in supercritical water, J. Supercrit. Fluid 50 (2009) 235–239.
[8] N. Zhang, H. Xu, B. Li, Y. Bai, D. Liu, Influence of the dissolved oxygen content on oxidation of ferritic–martensitic steel P92 in supercritical water, Corros. Sci. 56 (2012) 123–128.
[9] Y. Chen, K. Sridharan, T.R. Allen, Corrosion behavior of ferritic–martensitic steel T91 in supercritical water, Corros. Sci. 48 (2006) 2843–2854.
[10] X. Ren, K. Sridharan, T.R. Allen, Corrosion of ferritic–martenstic steel HT9 in supercritical water, J. Nucl. Mater. 358 (2006) 227–234.
[11] L. Tan, Y. Yang, T.R. Allen, Oxidation behavior of iron-based alloy HCM12A exposed in supercritical water, Corros. Sci. 48 (2006) 3123––3138.
[12] G.S. Was, P. Ampornrat, G. Gupta, S. Teysseyre, E.A. West, T.R. Allen, K. Sridharan, L. Tan, Y. Chen, X. Ren, C. Pister, Corrosion and stress corrosion cracking in supercritical water, J. Nucl. Mater. 371 (2007) 176–201.
[13] G.S. Was, T.R. Allen, Time, temperature, and dissolved oxygen dependence of oxidation of austenitic and ferritic–martensitic alloys in supercritical water, Proceeding of ICAPP'05 (2005), paper 5690.
[14] M. Bojinov, L. Heikinheimo, T. Siirio, S. Tuurna, Characterization of corrosion films on steels after long-term exposure to simulated supercritical water conditions, Proceedings of ICAPP'05 (2005) 1799–1807.
[15] J. Bischoff, A.T. Motta, Oxidation behaviour of ferritic–martensitic and ODS steels in supercritical water, J. Nucl. Mater. 424 (2012) 261–276.
[16] H. Xu, Z.L. Zhu, N.Q. Zhang, Oxidation of ferritic steel T24 in supercritical water, Oxid. Metals 82 (2014) 21–31.
[17] L. Tan, Y. Yang, T.R. Allen, Porosity prediction in supercritical water exposed ferritic/martensitic steel HCM12A, Corros. Sci. 48 (2006) 4234–4242.
[18] T. Maruyama, N. Fukagai, M. Ueda, K. Kawamura, Chemical potential distribution and void formation in magnetite scale formed in oxidation of iron at 823K, Mater. Sci. Forum 461–464 (2004) 807–814.
[19] Mitsutoshi Ueda, Kenichi Kawamura, Toshio Maruyama, Void formation in magnetite scale formed on iron at 823 K-elucidation by chemical potential distribution, Mater. Sci. Forum 522–523 (2006) 37–44.
[20] A. Atkinson, Transport processes during the growth of oxide films at elevated temperature, Rev. Mod. Phys. 57 (1985) 437–470.
[21] J. Bischoff, A. Motta, C. Eichfeld, R. Comstock, G. Cao, T. Allen, Corrosion of ferritic–martensitic steels in steam and supercritical water, J. Nucl. Mater. 441 (2013) 604–611.
[22] S.A. Bradford, Fundamentals of corrosion in gases, in: Metals Handbook, 9th ed., ASM International, Metals Park, OH, 1987, pp. 61–76.
[23] D. Gómez-Briceno, F. Blázquez, A. Sáez-Maderuelo, Oxidation of austenitic and ferritic/martensitic alloys in supercritical water, J. Supercrit. Fluid 78 (2013) 103–113.
[24] L. Tan, M.T. Machut, K. Sridharan, T.R. Allen, Corrosion behavior of a ferritic/martensitic steel HCM12A exposed to harsh environments, J. Nucl. Mater. 371 (2007) 161–170.
[25] N.J. Cory, T.M. Herrington, Kinetics of oxidation of ferrous alloys by super-heated steam, Oxid. Metals 28 (1987) 237–258.
[26] L. Martinelli, F. Balbaud-Célérier, A. Terlain, S. Delpech, G. Santarini, J. Favergeon, G. Moulin, M. Tabarant, G. Picard, Oxidation mechanism of a Fe–9Cr–1Mo steel by liquid Pb–Bi eutectic alloy (part II), Corros. Sci. 50 (2008) 2537–2548.
[27] P. Kofstad, High Temperature Corrosion, Elsevier Applied Science Publishers Ltd., London, 1988.
[28] L. Martinelli, F. Balbaud-Célérier, A. Terlain, S. Delpech, G. Santarini, J. Favergeon, G. Moulin, M. Tabarant, G. Picard, Oxidation mechanism of a Fe–9Cr–1Mo steel by liquid Pb–Bi eutectic alloy (part I), Corros. Sci. 50 (2008) 2523–2536.
[29] L. Martinelli, F. Balbaud-Célérier, A. Terlain, S. Delpech, G. Santarini, J. Favergeon, G. Moulin, M. Tabarant, G. Picard, Oxidation mechanism of a Fe–9Cr–1Mo steel by liquid Pb–Bi eutectic alloy (part III), Corros. Sci. 50 (2008) 2549–2559.
[30] J. Robertson, The mechanism of high temperature aqueous corrosion of steel, Corros. Sci. 29 (1989) 1275–1291.
[31] J. Robertson, The mechanism of high temperature aqueous corrosion of stainless steels, Corros. Sci. 32 (1991) 443–465.
[32] J. Topfer, S. Aggarwal, R. Dieckmann, Point defects and cation tracer diffusion in $(Cr_xFe_{1-x})_{3-\delta}O_4$ spinels, Solid State Ionics 81 (1995) 25–266.
[33] G.S. Was, S. Teysseyre, J. McKinley, Corrosion and stress corrosion cracking of iron- and nickel-base austenitic alloys in supercritical water, in: Proceeding of NACE Corrosion 2004, New-Orleans, LA, 2004, Paper 04492.
[34] M. Hänsel, W.J. Quadakkers, D.J. Young, Role of water vapor in chromia-scale growth at low oxygen partial pressure, Oxid. Metals 59 (2003) 285–301.
[35] D.J. Young, High Temperature Oxidation and Corrosion of Metals, Elsevier Science, 2008.
[36] L. Tan, X. Ren, T.R. Allen, Corrosion behavior of 9–12% Cr ferritic–martensitic steels in supercritical water, Corros. Sci. 52 (2010) 1520–1528.
[37] H.L. Hu, Z.J. Zhou, M. Li, L.F. Zhang, M. Wang, S.F. Li, C.C. Ge, Study of the corrosion behavior of a 18Cr-oxide dispersion strengthened steel in supercritical water, Corros. Sci. 65 (2012) 209–213.
[38] D. Laverde, T. Gómez-Acebo, F. Castro, Continuous and cyclic oxidation of T91 ferritic steel under steam, Corros. Sci. 46 (2004) 613–631.
[39] X.Y. Zhong, X.Q. Wu, E.H. Han, Effects of exposure temperature and time on corrosion behaviour of a ferritic–martensitic steel P92 in aerated supercritical water, Corros. Sci. 90 (2015) 511–521.
[40] X.Y. Zhong, X.Q. Wu, E.H. Han, The characteristic of oxide scales on T91 tube after long-term service in an ultra-supercritical coal power plant, J. Supercrit. Fluid 72 (2012) 68––77.
[41] N.H. Lee, S. Kim, B.H. Choe, D.I. Kwon, Failure analysis of a boiler tube in USC coal power plant, Eng. Fail. Anal. 16 (2009) 2031–2035.